Nanoscale

Direct imaging of interlayer-coupled symmetric and antisymmetric plasmon modes in graphene/hBN/graphene heterostructures

Journal:	*Nanoscale*
Manuscript ID	NR-COM-05-2021-003210.R1
Article Type:	Communication
Date Submitted by the Author:	04-Aug-2021

Complete List of Authors:	Hu, Cheng; Shanghai Jiao Tong University, Key Laboratory of Artificial Structures and Quantum Control (Ministry of Education), Shenyang National Laboratory for Materials Science, School of Physics and Astronomy; Collaborative Innovation Center of Advanced Microstructures, Deng, Aolin; Shanghai Jiao Tong University, Key Laboratory of Artificial Structures and Quantum Control (Ministry of Education), Shenyang National Laboratory for Materials Science, School of Physics and Astronomy Shen, Peiyue; Shanghai Jiao Tong University, Key Laboratory of Artificial Structures and Quantum Control (Ministry of Education), Shenyang National Laboratory for Materials Science, School of Physics and Astronomy Luo, Xingdong; Shanghai Jiao Tong University, Key Laboratory of Artificial Structures and Quantum Control (Ministry of Education), Shenyang National Laboratory for Materials Science, School of Physics and Astronomy Zhou, Xianliang; Shanghai Jiao Tong University, Key Laboratory of Artificial Structures and Quantum Control (Ministry of Education), Shenyang National Laboratory for Materials Science, School of Physics and Astronomy Wu, Tongyao; Shanghai Jiao Tong University, Key Laboratory of Artificial Structures and Quantum Control (Ministry of Education), Shenyang National Laboratory for Materials Science, School of Physics and Astronomy Huang, Xinyue; Shanghai Jiao Tong University, Key Laboratory of Artificial Structures and Quantum Control (Ministry of Education), Shenyang National Laboratory for Materials Science, School of Physics and Astronomy Dong, Yulong; Shanghai Jiao Tong University, Key Laboratory of Artificial Structures and Quantum Control (Ministry of Education), Shenyang National Laboratory for Materials Science, School of Physics and Astronomy Watanabe, Kenji; Natiaonal Institute for Materials Science, Optical and Electronic Materials Unit Taniguchi, Takashi; Busshitsu Zairyo Kenkyu Kiko, ; Gakko Hojin Kyoto Gakuen, Xie, Guibai; China Academy of Space Technology (Xi'an), National Key

	Laboratory of Science and Technology on Space Microwave Li, Xiaojun; China Academy of Space Technology (Xi'an), National Key Laboratory of Science and Technology on Space Microwave Liang, Qi; Shanghai Jiao Tong Univeristy, Instrumental Analysis Center Shi, Zhiwen; Shanghai Jiao Tong University, Key Laboratory of Artificial Structures and Quantum Control (Ministry of Education), Shenyang National Laboratory for Materials Science, School of Physics and Astronomy; Collaborative Innovation Center of Advanced Microstructures

Direct imaging of interlayer-coupled symmetric and antisymmetric plasmon modes in graphene/hBN/graphene heterostructures

Cheng Hu[1,2†], Aolin Deng[1,2†*], Peiyue Shen[1,2†], Xingdong Luo[1,2], Xianliang Zhou[1,2], Tongyao Wu[1,2], Xinyue Huang[1,2], Yulong Dong[1,2], Kenji Watanabe[3], Takashi Taniguchi[4], Guibai Xie[5], Xiaojun Li[5], Qi Liang[1,2], Zhiwen Shi[1,2*]

[1]Key Laboratory of Artificial Structures and Quantum Control (Ministry of Education), Shenyang National Laboratory for Materials Science, School of Physics and Astronomy, Shanghai Jiao Tong University, Shanghai, 200240, China.

[2]Collaborative Innovation Center of Advanced Microstructures, Nanjing, 210093, China.

[3]Research Center for Functional Materials, National Institute for Materials Science, 1-1 Namiki, Tsukuba 305-0044, Japan.

[4]International Center for Materials Nanoarchitectonics, National Institute for Materials Science, 1-1 Namiki, Tsukuba 305-0044, Japan.

[5]National Key Laboratory of Science and Technology on Space Science, China Academy of Space Technology (Xi'an), Xi'an, China.

† These authors contribute equally to this work.

* To whom correspondence should be addressed. Email: zwshi@sjtu.edu.cn, daolin@sjtu.edu.cn.

Abstract:

Much of the richness and variety of physics today are based on coupling phenomena where multiple interacting systems hybridize into new ones with completely distinct attributes. Recent development in building van der Waals (vdWs) heterostructures from different 2D materials provides exciting possibilities in realizing novel coupling phenomena in a designable manner. Here, with a graphene/hBN/graphene heterostructure, we report near-field infrared nano-imaging of plasmon-plasmon coupling in two vertically separated graphene layers. Emergent symmetric and anti-symmetric coupling modes are directly observed simultaneously. Coupling and decoupling processes are systematically investigated with experiment, simulation and theory. The reported interlayer plasmon-plasmon coupling could serve as an extra degree of freedom to control light propagation at the deep sub-wavelength scale with low loss and provide exciting opportunities for optical chip integration.

1. Introduction

Many intriguing physical phenomena emerged from coupling effects, such as Fano resonance[1-3], Rabi oscillation[4, 5] and formation of Cooper pairs[6]. Owing to the recent development of transfer technique in low dimensional materials[7, 8], it is feasible and convenient to fabricate various Van der Waals heterostructures with different 2D materials. Such heterostructures provide an ideal platform to study coupling phenomena of particles or quasi-particles from different layers with precise control. Recently, many new physical processes and phenomena have been discovered in the 2D heterostructures. For instance, interlayer coupling through moiré potential between the graphene and hBN layers leads to mini-Dirac cones and the Hofstadter's butterfly pattern in graphene/hBN heterostructures[9-14]; interlayer electron-phonon coupling can activate optically silent hBN phonons in Raman spectra of WSe_2/hBN heterostructures[15]; interlayer electron-electron coupling leads to a flat electronic band and gives rise to superconductivity and Mott insulating states in magic angle twisted bilayer graphene[16-19].

Plasmon polaritons in an individual layer of graphene have already attracted tremendous attention due to its advantages in tunability, long-lifetime and extreme spatial confinement. Such advantages of graphene plasmons benefit from the unique Dirac-cone band structure of graphene, which is typically unavailable in metal nanostructures. Interesting coupling phenomena, including plasmon-phonon[20] and plasmon-exciton[21] have been observed in graphene. In addition, plasmon-plasmon coupling between graphene and other metal nanostructures has also been studied and many novel physical processes are discovered[22-24]. However, the most emblematic plasmon-plasmon coupling and decoupling in two vertically separated identical graphene sheets has only been investigated theoretically[25] and is lack of experimental realization.

For the simplest coupling configuration with two graphene layers being placed close to each other, two single-layer plasmon modes with the same wavelength start to overlap and evolve into two new eigen modes: one symmetric mode and one anti-

symmetric mode with respect to their charge distributions. Here by symmetric mode, we mean that the charge distribution is the same in two layers—conversely the anti-symmetric mode corresponds to opposite charge distribution in two layers.

Here, using a homemade scanning near-field optical microscope (SNOM)[26-28], we studied plasmon-plasmon coupling in two graphene sheets separated by an isolating layer of hBN. Symmetric and anti-symmetric plasmon modes were directly imaged simultaneously for the first time in both the strong and weak coupling regimes. Combining with finite element simulation and theoretical analysis, we systematically investigated the coupling and decoupling processes of graphene plasmons in two separated graphene sheets. The plasmon-plasmon coupling provides an extra degree of freedom to tune graphene plasmons and reduce the electromagnetic loss in the deep sub-wavelength scale and therefore is suitable for manufacturing tunable nanophotonic devices.

2. Results and discussion

Fig. 1(a) shows the schematic of our device structure and the near-field infrared measurement. The device consists of top-layer graphene, bottom-layer graphene, and a dielectric hBN layer in the middle, sitting on a SiO_2/Si substrate. The two layers of graphene and the silicon back gate are connected to electrodes individually. Two gate voltages U_1 and U_2, as shown in Fig. 1(b), are applied to the device to independently control both top- and bottom-layer graphene Fermi energies. When the two graphene layers are charged with equal number of electrons and holes, respectively, as illustrated in Fig. 1(b), the plasmon wavelengths of the two layers will be the same and therefore the plasmon-plasmon coupling strength will reach a maximum. The device contains both top- and bottom-layer graphene overlapped region as well as the non-overlapped region. The advantage of this configuration is that we can measure the plasmon wavelength of both the uncoupled modes and the coupling modes simultaneously, which enables us to study the coupling induced change of plasmon wavelength. The uncoupled single-layer plasmon wavelength is measured from the non-overlapped top-

and bottom-layer graphene, while the wavelength of coupling mode is achieved from the overlapped region. Based on a recent study of the non-local electrostatic gating effect in graphene, the Fermi level of graphene tuned by a local gate features almost uniform across the whole graphene flake due to the quantum capacitance of graphene and electrostatic screening from absorbed polar molecules[29]. As a result, the plasmon wavelengths in different regions (overlapped and non-overlapped regions) will be the same if plasmon-plasmon coupling induced change in the overlapped region can be neglected. This is confirmed by direct observation of the same wavelength in overlapped and non-overlapped regions when the bottom-layer graphene is at charge neutral or the bottom-layer graphene is vertically far away from the top-layer graphene (See Fig. S3 and S4). Therefore, the plasmon wavelength measured in the non-overlapped graphene region can well represent the uncoupled plasmon wavelength of the overlapped region. Based on this, we can compare the plasmon wavelength of the uncoupled mode with the coupling modes and study the plasmon-coupling induced change.

Both the coupled and the uncoupled plasmon modes are observed simultaneously through near-field nano-imaging. Fig. 1(c) shows the near-field image of Device 1, in which plasmon wavelengths of the two graphene layers are tuned to be the same. The thickness of dielectric hBN layer is 12 nm, which is thick enough to avoid interlayer electron tunneling[30, 31] and therefore only plasmon-plasmon interaction need to be considered. The top-layer graphene, bottom-layer graphene and the overlapped region are denoted in Fig. 1(c) and its boundaries are mark by dotted line. The overlapped region possesses a stronger near-field response than the individual graphene layers and displays brighter in the IR image. In addition, the period of the plasmon interference pattern in the overlapped region is also different from that of the individual layer. We extract the plasmon profile from the overlapped region, isolated top-layer and bottom-layer graphene, and present them in Fig. 1(d). While that of non-overlapped top- and bottom-layer graphene mainly shows a gradually decayed sinusoidal lineshape with a wavelength of 150 nm, the plasmon profile of the overlapped region shows a rather

strange lineshape that can not be described by a single sinusoidal function. To see it more clearly, we performed Fourier transform (FT) of the line profile in the overlapped region and plotted it in Fig. 1(e). Two prominent peaks can be observed: one with wavenumber lower than k_{p} (the wavevector of the individual-layer graphene plasmon, $k_{\mathrm{p}} = 2\pi/\lambda_{\mathrm{p}}$. See Fig. S1), denoted as β_- mode; the other one with wavenumber higher than k_{p}, denoted as β_+ mode. Presumably, the two new modes correspond to the symmetric- and antisymmetric-coupled plasmon modes.

To confirm that the experimentally observed β_- and β_+ modes are indeed symmetric and anti-symmetric coupling modes, we carried out numerical simulation using the finite element method (see more details in supplementary information). The simulation model consists of five layers from top to bottom: air, graphene, hBN, graphene, and SiO_2, which corresponds exactly to the structure of the overlapped region of our device. In our simulation, a dynamic electric dipole was chosen to serve as the 10.6 um laser source to excite plasmons in graphene. The simulated near-field distribution of the transverse electric field is shown in Fig. 2(a), from which two eigen modes can be extracted: one with a longer wavelength and smaller wavenumber (β_-), the other one with a shorter wavelength and larger wavenumber (β_+). The charge distribution of β_- mode is symmetric with respect to the center plane of the heterostructure, whereas that of β_+ mode is anti-symmetric. Such modes are similar to the coupled plasmon modes in a metal-insulator-metal waveguide (See supplementary information for more details). The transverse electric field of the symmetric mode β_- is mainly distributed outside the two graphene layers, while that of the anti-symmetric mode β_+ is mainly concentrated in between the two graphene layers. Therefore, it is typically more difficult to detect the β_+ mode with the SNOM technique[31]. To analysis the field decay of the two coupling modes, we made three lines cut at different heights of $0.1\lambda_{\mathrm{p}}$, $0.2\lambda_{\mathrm{p}}$ and $0.5\lambda_{\mathrm{p}}$ in Fig. 2(a) and plotted the simulated near-field line profiles in Fig. 2(b). Near the surface at $\mathrm{h}_1 = 0.1\lambda_{\mathrm{p}}$, the line profile exhibits a rather complicated shape due to the interference between β_- and β_+

modes. Presumably, the short-wavelength β_+ mode decays much faster than the long-wavelength β_- mode due to reduced wavelength. Indeed, the composite line profile gradually transforms into a simple sinusoidal line shape containing only β_- mode at $h_3 = 0.5\lambda_p$. To analyze the speed of the field decay, we then carried out the Fourier transform of the three electric field line profiles and plotted them in Fig. 2(c), in which two prominent peaks show up, corresponding to the β_- and β_+ modes respectively. The two peaks coincide well with the experimental peaks in Fig. 1(e), confirms the coupling induced symmetric and anti-symmetric modes observed in the near-field infrared images. With increasing the detection distance, the amplitude of both modes decreases, but the β_+ with smaller wavelength decays much faster, which is clearly displayed in the inset of Fig. 2(c). This can explain the fact that the long wavelength β_- dominants in the experimental near-field infrared images. More quantitatively, the longitudinal electric field of both modes decays exponentially following $E = E_{0,\pm} e^{-\beta_\pm \cdot z}$ and the decay factors of the two modes are $\lambda_-/2\pi$ and $\lambda_+/2\pi$, respectively. In our near-field scanning, the AFM tip is tapping with an amplitude of about 50 nm, corresponding to an average tip-sample distance of 25 nm, which is about $0.15\lambda_p$. Therefore, it is feasible to observe both β_- and β_+ modes in our experiment.

As we have confirmed the observed symmetric and anti-symmetric coupling modes, it is of great importance to explore the evolution of coupling in different coupling regimes, which is experimentally realized here by altering the thickness of the dielectric hBN layer. We first define a coupling factor $g = k_p \cdot d$ to differentiate coupling situations, where k_p is the single layer graphene plasmon wavenumber and d is the hBN thickness, respectively. The situation of $g \ll 1$ corresponds to strong coupling, and $g \geq 1$ the weak coupling. The following results discussed using g-factor would be general to plasmons of other wavelengths because g is dimensionless and scale uncorrelated. Experimental near-field distribution of different coupling g factors (controlled by choosing different thickness d of the separating hBN layer) is shown in Figs. 3(a)-(d). Note that we have adjusted gate voltages U_1 and U_2 to ensure that ~~the Fermi level, as well as~~ the intrinsic plasmon wavelength in both layers is the same, since

only in this case the coupling reaches a maximum and the g factor can be well defined. We found the line profile evolutions from the strong to weak coupling traverse roughly three regimes in the near-field images. In the strong coupling regime (g ≈ 0.2, devices 2 with d = 3 nm, Fig. 3(a)), the oscillated charges in the different graphene layers are close, which causes the β_- and β_+ modes to split drastically. The β_+ mode with opposite sign charges in the two graphene layers neutralizes the electric field in a very short height from the top layer graphene surface, which leads this mode to disappear in the near-field image, as shown in Fig. 3(e) (field line profile in real space) and Fig. 3(i) (eigen modes in frequency domain). Therefore, only the long-wavelength β_- mode is observed in the strong coupling regime. With the coupling factor g increasing, the plasmon-plasmon coupling becomes weaker (g ≈ 0.3, 0.5, device 3 with d = 8 nm, and device 1 with d = 12 nm, Figs. 3(b), (c)), the wavelength of β_+ mode increases and starts to appear in the near-field images. Figs. 3(f), (g) and 3(j), (k) (g ≈ 0.3, 0.5) show the coupling modes in real space and frequency domain. In weak coupling regime (Fig. 3(d)), the difference of the two coupling modes become smaller, which caused the two modes almost combine into one peak, as shown in Fig. 3(h) and 3(l) (g ≈ 0.9, device 4 with d = 20 nm). Numerical simulation also shows a systematic evolution of the two coupling modes under different coupling factor g (see more simulation details in Methods), as shown in Fig. 3(m) and Fig. S2. With coupling factor g decreasing, two coupling modes (β_- and β_+) are getting more separated, as indicated by the bright lines. Experimentally extracted coupling modes are also dotted in Fig. 3(m), which match quite well with the numerical simulation. Here we would like to emphasize that comparing with the single-layer graphene plasmon the short-wavelength anti-symmetric β_+ mode not only shows a stronger spatial confinement, but also exhibits a slightly higher Q-factor (see more details in Supplementary Materials), which are two key figures of merit for plasmonics and are highly desirable for building the novel plasmonic devices.

To better understand the peculiar coupling modes, we employ a theoretical model[32]. The permittivity of graphene is given by $\varepsilon_g = 1 + i\sigma_g\eta_0/(k_0\Delta)$, where σ_g is the

surface conductivity of graphene, η_0 the air impedance, Δ the graphene thickness and k_0 the wavevector of excitation light in free-space. For simplicity, we use an average dielectric constant ε_s to describe the surrounding dielectric environment of graphene plasmons. Here, we only consider the TM polarized plasmons. Therefore, we can generate electric fields in different regions of our graphene system according to the traditional waveguide theory. By matching the boundary conditions that the transverse electric fields are continuous at the interfaces and figuring out the limit as Δ close to zero, the dispersion relation of the coupling mode can be achieved as[32],

$$-k_s\left(\pm e^{-k_s d}-1\right)=\frac{2i\varepsilon_s k_0}{\eta_0\sigma_g} \quad (1)$$

where $k_s=\sqrt{\beta^2-\varepsilon_s k_0^2}$, β is the coupling modes wave vector. By solving equation (1) numerically, we achieve the evolution of the two modes from strong to weak coupling regimes, as shown in Fig. 3(n), where the purple and cyan lines indicate the β_- and β_+ modes, respectively. In the strong coupling regime, mode splitting is significant in the frequency domain and differs from the meristic separate in the weak coupling regime. The β_- mode frequency increases much faster than the β_+ mode decreases. Such qualitative feature is also confirmed by the simulation results in Fig. 3(m). The quantitative difference between the analytical and numerical results comes from the assumption of uniform dielectric and zero thickness of graphene. For the β_+ mode, the matches of analytical and numerical results are quite well even in the strong coupling regime. Note that at strong coupling the velocity of β_+ mode plasmon can be close to the electron Fermi velocity, indicating that this coupled graphene plasmon system provides a platform to explore new physics at extreme confinement.

More interestingly, we found the observed plasmon-plasmon coupling is analogous to a coupled two-level quantum system. Considering a system with two separated quantum wells, each quantum well has its own ground state energy E_0. When these two quantum wells are moving close, the two single-well ground states start to interact with each other and evolve into two new eigen modes—one symmetric mode and one anti-symmetric mode. Using this picture, we can also solve the plasmon-plasmon coupling

and work out the wavevector of the symmetric and anti-symmetric plasmon modes (see more details in Supplementary Materials). The calculated result is shown in Fig. 3(n) with gray lines, which also matches qualitatively with our experimental data.

The results discussed above correspond to the case that both the top- and bottom-layers have the same charge density and the same intrinsic plasmon wavelength. In a more common situation, the charge density of the two graphene layers is unequal, which leads to different plasmon wavelengths in the top- and bottom-layers. The difference in plasmon wavelength will cause a phase mismatch. As a result, the plasmon-plasmon coupling strength will decrease. Therefore, it is necessary to introduce the decoupling process to understand the coupling phenomenon more comprehensively. We experimentally tuned the Fermi level of two graphene layers in Device 1 away from each other through adjusting the two gate voltages U_1 and U_2. The tuned Fermi energy of two graphene layers is then described by $E_F = E_{F0} \pm \Delta|E_F|/2$, as illustrated in Fig. 4(a). For $\Delta|E_F|$ = 0.14 eV, plasmon line profiles in the overlapped region, non-overlapped top-layer region, and non-overlapped bottom-layer region of Device 1 are displayed in Fig. 4(b). The plasmon wavelength of top-layer graphene is decreased to 122 nm, while that of the bottom-layer graphene is increased to 181 nm, showing a remarkable detuning in plasmon wavelength. The line-profile of resulted coupling-modes (black line in Fig. 4(b)) from the two detuned plasmons looks quite different from those coupling modes with no detuning (Fig. 3(e)-(h)). Its Fourier transform is shown in Fig. 4(c), where two well-defined coupling modes can still be identified. The two modes correspond to the anti-symmetric (β_+) and symmetric (β_-) modes as before, rather than the individual layer modes, k_b (bottom layer) or k_t (top layer), which are denoted by two dashed lines. Note that the frequency of the coupled β_+ mode is higher than the high frequency non-interacting mode (k_t), and that of the β_- mode is lower than the low frequency non-interacting mode (k_b). Such a coupling induced shift of mode frequency is also similar to that of the interacting two-level quantum system model. We also performed numerical simulation for the detuning process. In the simulation model, we set the initial Fermi energy of the two graphene

layers $E_{F0} = 0.43$ eV and the coupling factor $g \approx 0.5$. We equally increased and decreased the graphene Fermi energy in different layers with $\Delta|E_F|/2$, which introduced a difference in the plasmon wavelength between the top- and bottom-layer graphene $|\lambda_b - \lambda_t|$. The simulation results in the frequency domain are shown in Fig. 4(d). The white dashed curves in this figure show the uncoupled intrinsic plasmon wavevector in both graphene layers, and the experiment data is dotted in the figure. With wavelength difference $|\lambda_b - \lambda_t|$ increasing, the β_- and β_+ modes are getting closer to the uncoupled plasmon mode of monolayer graphene, revealing a definite decoupling process.

3. Conclusion

We have directly observed interlayer coupling induced symmetric and anti-symmetric plasmon modes in graphene/hBN/graphene heterostructures using SNOM technique. Combining with numerical simulation and theoretical analysis, we systematically investigate the coupling phenomena from strong to weak coupling regimes, as well as the decoupling processes induced by wavelength detuning. Interestingly, the coupled symmetric and anti-symmetric plasmon modes can also be resolved using an interacting two-level quantum system model. The observed interlayer plasmon coupling provides a unique way to efficiently control the plasmon wavelength and reduce the electromagnetic loss at deep sub-wavelength scale and open up a new way to investigate the quasi-particle interaction, which are attractive for building nanophotonic devices and circuits.

4. Experimental section

Sample fabrication

The bottom-layer graphene was mechanically exfoliated on the silica substrate. The isolator layer hBN and top-layer graphene were transferred onto the graphene one by one by the dry transfer methods. After each transfer steps, the sample was annealed in

the hydrogen plasmon at the temperature of 300 ℃ to get rid of the adhesive residues. The power of plasma was 30 W and the flow of H_2 was 35 SCCM with a pressure of about 47 Pa. The distance between our sample and the center of the coil was about 45 cm. All the electrodes (50 nm Au/3 nm Ti) were fabricated by electronic beam evaporation.

Infrared nano-imaging

Our home-made scattering-type SNOM setup was based on a commercial AFM (Bruker Innova). A beam of CO_2 laser with 10.6 μm wavelength was illuminated onto a gold-coated AFM tip, which generated a near-field hot spot at the nanometer-scale tip apex. Such a largely confined hot spot could provide extra momentum and excited plasmons in graphene. The excited plasmons propagated and got reflected at the graphene edges. The reflected plasmons modulated the local field at the tip apex and changed the light scattering that was recorded by an MCT detector placed in the far field. Plasmon interference pattern could be obtained when scanning over the graphene. In order to suppress background scattering from the cantilever and the sample, the tip was vibrated vertically with an amplitude of ~50 nm at a frequency of about 200 kHz, and the detector signal was demodulated at a higher order harmonic frequency by a lock-in amplifier (Zurich Instruments, HF2LI).

COMSOL simulation

Numerical simulations were conducted using the wave optics module of the commercial software package COMSOL. We only focused on the electric field component normal to the surface of the sample (E_z). The max mesh size was limit within 2 nm in all the simulation situations to get the convergent results. Unless otherwise stated, the electric field monitor was located at a height of 1 nm from the top-layer graphene. More details can be seen in the supplementary information. The distribution of the electric field of symmetric (β_-) and antisymmetric (β_+) modes are solved by the COMSOL mode analyzer in the Wave Optics Module in the frequency domain. By setting device structure and boundary configuration the same as in our experiments, the mode analyzer can find out all the eigen modes of plasmons that can be supported in our device

structure. Then, we manually select the fundamental modes with symmetrically and antisymmetrically distributed charge and neglect all other higher order modes.

Conflicts of interest

There are no conflicts to declare.

Author contributions

Z.S. and A.D. conceived this project. A.D. and P.S. prepared the heterostructure samples and performed the near-field infrared measurements. C.H. carried out the COMSOL simulations. K.W. and T.T. provided the hBN crystals. C.H., A.D., P.S., X.L., X.Z. and Z.S. analyzed the data. C.H., A.D. and Z.S. wrote the paper with inputs from all authors.

Acknowledgements

This work is supported by the National Key Research and Development Program of China (2016YFA0302001) and the National Natural Science Foundation of China (11774224, 11574204 and 61701394). Z.S. acknowledges support from the Program for Professor of Special Appointment (Eastern Scholar) at Shanghai Institutions of Higher Learning. K.W. and T.T. acknowledge support from the Elemental Strategy Initiative conducted by the MEXT, Japan, Grant Number JPMXP0112101001, JSPS KAKENHI Grant Number JP20H00354 and the CREST (JPMJCR15F3), JST. We would also like to thank the Centre for Advanced Electronic Materials and Devices (AEMD) of Shanghai Jiao Tong University (SJTU) for the support in device fabrication.

References

1. B. Luk'yanchuk, N. I. Zheludev, S. A. Maier, N. J. Halas, P. Nordlander, H. Giessen and C. T. Chong, *Nature Materials*, 2010, **9**, 707-715.

2. P. Fan, Z. Yu, S. Fan and M. L. Brongersma, *Nature Materials*, 2014, **13**, 471-475.

3. C. Handschin, P. Makk, P. Rickhaus, M.-H. Liu, K. Watanabe, T. Taniguchi, K. Richter and C. Schönenberger, *Nano Letters*, 2017, **17**, 328-333.

4. Y. O. Dudin, L. Li, F. Bariani and A. Kuzmich, *Nature Physics*, 2012, **8**, 790-794.

5. K. Shandarova, C. E. Rüter, D. Kip, K. G. Makris, D. N. Christodoulides, O. Peleg and M. Segev, *Physical Review Letters*, 2009, **102**, 123905.

6. S. Komori, J. M. Devine-Stoneman, K. Ohnishi, G. Yang and J. Robinson, *Sci Adv*, 2021, **7**, eabe0128.

7. F. Pizzocchero, L. Gammelgaard, B. S. Jessen, J. M. Caridad, L. Wang, J. Hone, P. Bøggild and T. J. Booth, *Nature Communications*, 2016, **7**, 11894.

8. L. Wang, I. Meric, P. Y. Huang, Q. Gao, Y. Gao, H. Tran, T. Taniguchi, K. Watanabe, L. M. Campos, D. A. Muller, J. Guo, P. Kim, J. Hone, K. L. Shepard and C. R. Dean, *Science*, 2013, **342**, 614.

9. M. Yankowitz, J. Xue, D. Cormode, J. D. Sanchez-Yamagishi, K. Watanabe, T. Taniguchi, P. Jarillo-Herrero, P. Jacquod and B. J. LeRoy, *Nature Physics*, 2012, **8**, 382-386.

10. B. Hunt, J. D. Sanchez-Yamagishi, A. F. Young, M. Yankowitz, B. J. LeRoy, K. Watanabe, T. Taniguchi, P. Moon, M. Koshino, P. Jarillo-Herrero and R. C. Ashoori, *Science*, 2013, **340**, 1427.

11. C. R. Dean, L. Wang, P. Maher, C. Forsythe, F. Ghahari, Y. Gao, J. Katoch, M. Ishigami,

P. Moon, M. Koshino, T. Taniguchi, K. Watanabe, K. L. Shepard, J. Hone and P. Kim, *Nature*, 2013, **497**, 598-602.

12. L. A. Ponomarenko, R. V. Gorbachev, G. L. Yu, D. C. Elias, R. Jalil, A. A. Patel, A. Mishchenko, A. S. Mayorov, C. R. Woods, J. R. Wallbank, M. Mucha-Kruczynski, B. A. Piot, M. Potemski, I. V. Grigorieva, K. S. Novoselov, F. Guinea, V. I. Fal'ko and A. K. Geim, *Nature*, 2013, **497**, 594-597.

13. W. Yang, G. Chen, Z. Shi, C.-C. Liu, L. Zhang, G. Xie, M. Cheng, D. Wang, R. Yang, D. Shi, K. Watanabe, T. Taniguchi, Y. Yao, Y. Zhang and G. Zhang, *Nature Materials*, 2013, **12**, 792-797.

14. Z. Shi, C. Jin, W. Yang, L. Ju, J. Horng, X. Lu, H. A. Bechtel, M. C. Martin, D. Fu, J. Wu, K. Watanabe, T. Taniguchi, Y. Zhang, X. Bai, E. Wang, G. Zhang and F. Wang, *Nature Physics*, 2014, **10**, 743-747.

15. C. Jin, J. Kim, J. Suh, Z. Shi, B. Chen, X. Fan, M. Kam, K. Watanabe, T. Taniguchi, S. Tongay, A. Zettl, J. Wu and F. Wang, *Nature Physics*, 2017, **13**, 127-131.

16. Y. Cao, V. Fatemi, S. Fang, K. Watanabe, T. Taniguchi, E. Kaxiras and P. Jarillo-Herrero, *Nature*, 2018, **556**, 43-50.

17. Y. Cao, V. Fatemi, A. Demir, S. Fang, S. L. Tomarken, J. Y. Luo, J. D. Sanchez-Yamagishi, K. Watanabe, T. Taniguchi, E. Kaxiras, R. C. Ashoori and P. Jarillo-Herrero, *Nature*, 2018, **556**, 80-84.

18. M. Yankowitz, S. Chen, H. Polshyn, Y. Zhang, K. Watanabe, T. Taniguchi, D. Graf, A. F. Young and C. R. Dean, *Science*, 2019, **363**, 1059.

19. E. Codecido, Q. Wang, R. Koester, S. Che, H. Tian, R. Lv, S. Tran, K. Watanabe, T.

Taniguchi, F. Zhang, M. Bockrath and C. N. Lau, *Science Advances*, 2019, **5**, eaaw9770.

20. D. Yoo, F. d. León-Pérez, M. Pelton, I. H. Lee and S. H. Oh, *Nat Photonics*, 2021, **15**, 1-6.

21. J. H. Zhong, J. Vogelsang, J. M. Yi, D. Wang and C. Lienau, *Nat Commun*, 2020, **11**.

22. S. Zhang, D. A. Genov, Y. Wang, M. Liu and X. Zhang, *Phys Rev Lett*, 2008, **101**, p.218-221.

23. A. Artar, A. A. Yanik and H. Altug, *Nano Letters*, 2011, **11**, 1685-1689.

24. C. Hu, L. Wang, Q. Lin, X. Zhai, X. Ma, T. Han and J. Du, *Applied Physics Express*, 2016, **9**, 052001.

25. B. Wang, X. Zhang, X. Yuan and J. Teng, *Applied Physics Letters*, 2012, **100**.

26. R. HillenbRand, B. Knoll and F. Keilmann, *Journal of Microscopy*, 2001, **202**, 77-83.

27. Z. Fei, A. S. Rodin, G. O. Andreev, W. Bao, A. S. McLeod, M. Wagner, L. M. Zhang, Z. Zhao, M. Thiemens, G. Dominguez, M. M. Fogler, A. H. Castro Neto, C. N. Lau, F. Keilmann and D. N. Basov, *Nature*, 2012, **487**, 82-85.

28. J. Chen, M. Badioli, P. Alonso-González, S. Thongrattanasiri, F. Huth, J. Osmond, M. Spasenović, A. Centeno, A. Pesquera, P. Godignon, A. Zurutuza Elorza, N. Camara, F. J. G. de Abajo, R. Hillenbrand and F. H. L. Koppens, *Nature*, 2012, **487**, 77-81.

29. A. Deng, C. Hu, P. Shen, X. Luo, J. Chen, B. Lyu, K. Watanabe, T. Taniguchi, Q.-F. Liang, J. Ma and Z. Shi, 2021. arXiv:2103.16097

30. R. V. Gorbachev, A. K. Geim, M. I. Katsnelson, K. S. Novoselov, T. Tudorovskiy, I. V. Grigorieva, A. H. Macdonald, S. V. Morozov, K. Watanabe and T. Taniguchi, *Nat Phys*,

2012. **8**(12), 896-901

31. A. Woessner, A. Misra, Y. Cao, I. Torre, A. Mishchenko, M. Lundeberg, K. Watanabe, T. Taniguchi, M. Polini and K. Novoselov, *Acs Photonics*, 2017, **4**(12), 3012-3017.

32. B. Wang, X. Zhang, X. Yuan and J. Teng, *Appl Phys Lett*, 2012, **100**(13), 131111

Figures and figure captions

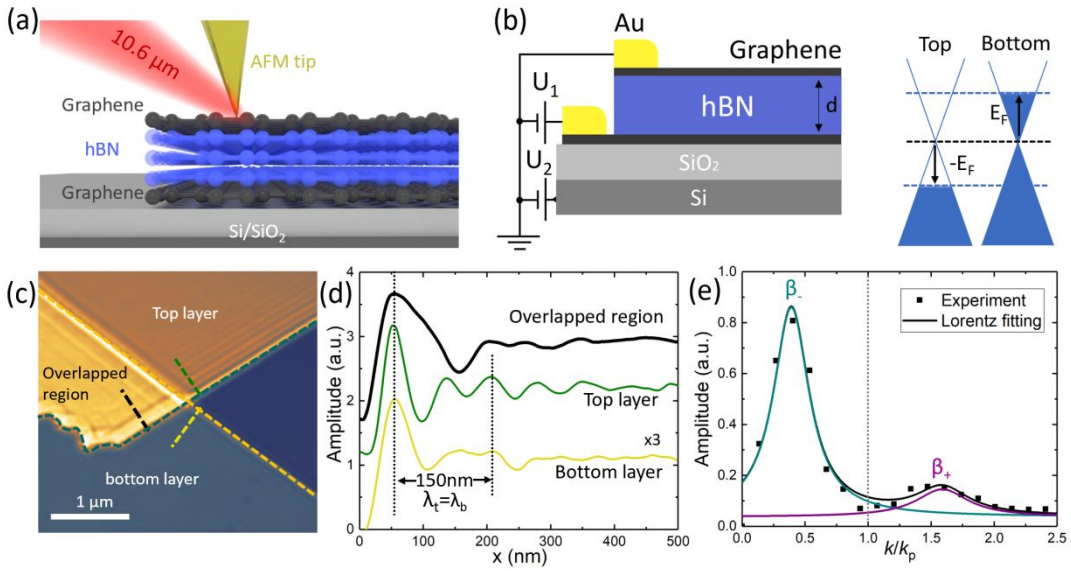

Fig. 1 (a) Schematic diagram of SNOM measurement of interlayer-coupled plasmons. (b) The device structure and the Fermi level of the two graphene layers. (c) Near-field infrared imaging of both individual-layer plasmons and interlayer-coupled plasmons. The dotted lines marked the boundary of top (green) and bottom (orange) layer graphene. (d) The near-field line profile extracted from the black (overlapped region), green (top-layer graphene) and yellow (bottom-layer graphene) lines in (c). (e) Modes amplitude of inter-layer coupled plasmons. The experimental dots are Furrier transform of the black line in (d). The lines are Lorentz fitting. Two modes can be clearly seen: one with a smaller wavevector (β_-), and the other one with a larger wavevector (β_+), in comparing with the individual layer plasmon mode.

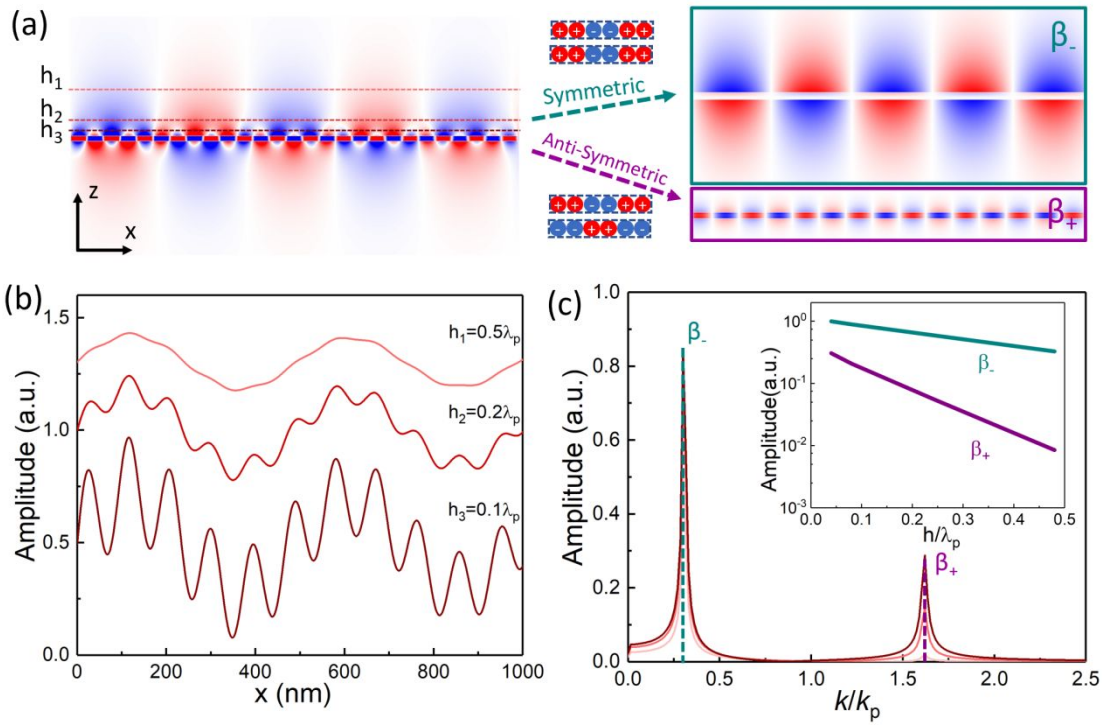

Fig. 2 (a) Simulated near-field ($\boldsymbol{E}_z$) distribution in the heterostructure, which can be decomposed into a symmetric (β_-) and an anti-symmetric (β_+) mode. (b) The simulated near-field line profiles at different heights denoted in (a). (c) Mode amplitude obtained through Fourier transform of the lines in (b). The insert shows the decay of the modes with increasing the probe distance, where the mode β_+ with a shorter wavelength decays much faster than the β_- mode.

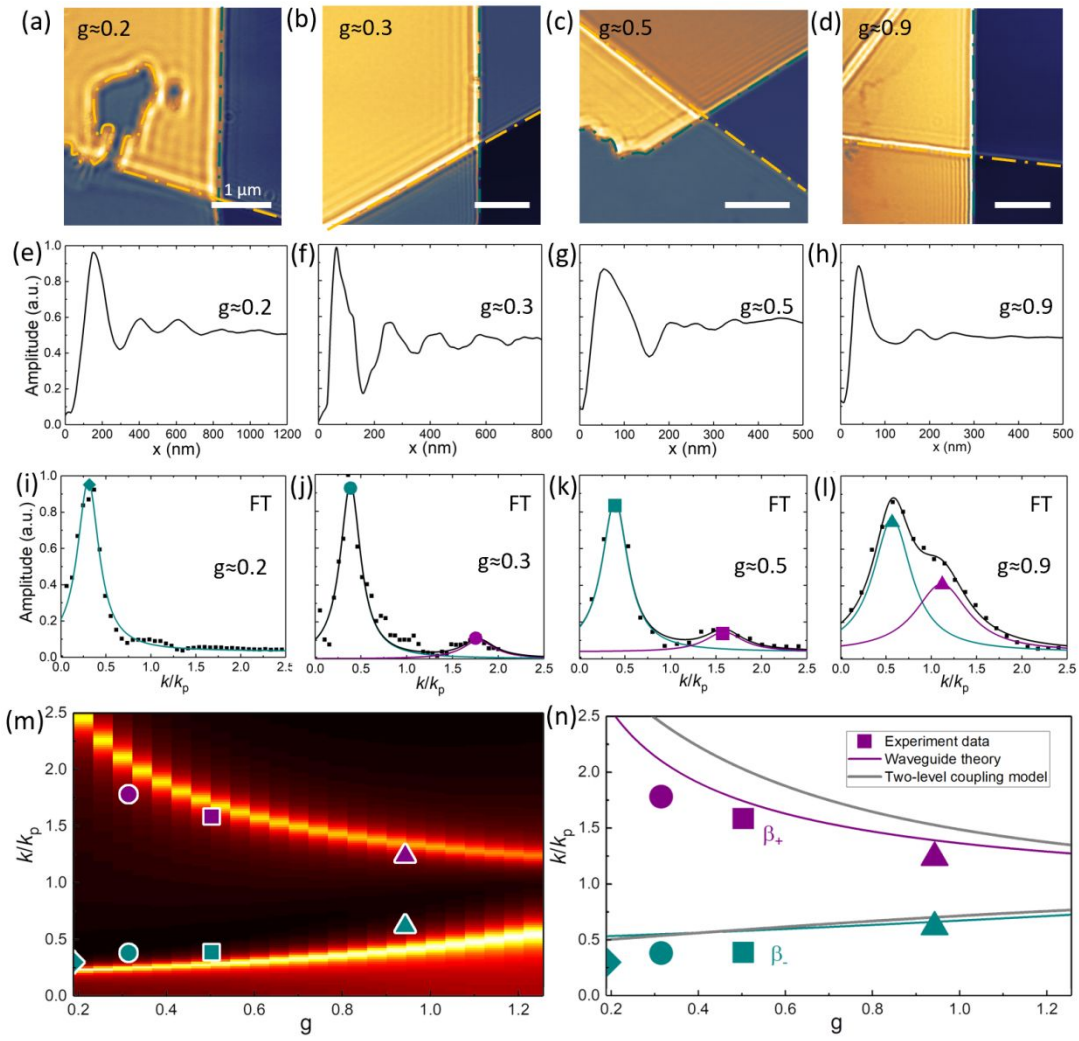

Fig. 3 (a)-(d) Near-field infrared nanoimaging of coupled plasmons with different coupling factor g. Scale bars: 1 μm. (e)-(h) The line profile of coupled plasmons with different coupling factors. (i)-(l) The corresponding Fourier transform of the near-field line profile in (e)-(h). The solid lines are the Lorentz fitting of the experiment data (black dots). (m) Numerical simulation of the interlayer coupled modes as a function of the coupling factors g. (n) Theoretical solution of the coupled symmetric and anti-symmetric modes at different coupling factors g. The purple and green dots are the β_+ and β_- modes extracted from experiment data in (i)-(l). The gray lines are fitted by using the coupled two-level quantum model.

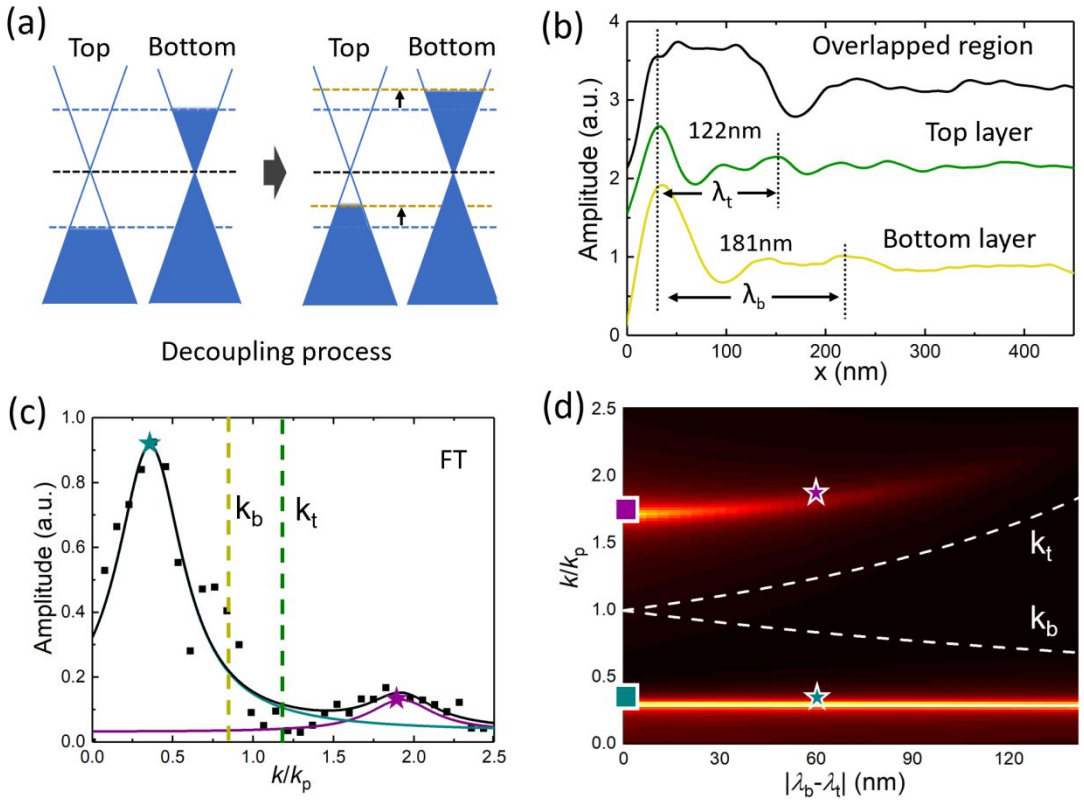

Fig. 4 (a) Decoupling process by introducing a difference in plasmon wavelength (as well as in $|E_F|$) in the two graphene layers. (b) Near-field line profiles in overlapped region, top-layer, and bottom-layer of Device 1 when $\Delta|E_F| = 0.14$ eV. (c) Fourier transform of the near-field line profile in the overlapped region. The black dots and solid lines correspond to experiment data and Lorentz fitting, respectively. (d) The numerical simulation of the decoupling process: as the difference in plasmon wavelength of the two layers increasing, the plasmon coupling becomes weaker. As a result, the coupled modes are moving closer to the individual-layer modes, revealing a decoupling. The white lines indicate the top and bottom layer plasmon wavevectors.